Rigorous coupled-wave analysis equivalent-index-slab method for analyzing 3D angular misalignment in interlayer grating couplers

Congshan Wan,* Thomas K. Gaylord, and Muhannad S. Bakir

School of Electrical and Computer Engineering, Georgia Institute of Technology, Atlanta, Georgia 30332, USA
*Corresponding author: cwan3@gatech.edu

The interlayer waveguide grating coupling efficiencies under angular (rotational) misalignments are simulated using the 3D rigorous coupled-wave analysis (3D-RCWA) together with the RCWA equivalent-index-slab (RCWA-EIS) method. As examples of conical diffraction, rotations about the two coordinate axes, x and z, defined by the vectors [1 0 0] and [0 0 1], respectively, as well as an arbitrary axis, defined by the vector [2 2 1], are simulated for binary rectangular-groove gratings. The interlayer grating coupling efficiency is approximated by the product of the top- and bottom-grating diffraction efficiencies (DEs). It is found that the bottom-grating DEs decrease about 25% when the bottom grating is rotated ±0.1 rad (5.73°) about the z-axis. DEs slightly increase (5% to 10% depending on the grating structures) when the bottom grating is rotated ±0.1 rad about the x-axis. This is consistent with the diffraction behavior of an over-modulated grating. When the bottom grating is rotated about the vector [2 2 1], the change in DEs is asymmetric with a 100% decrease at a rotation angle –0.1 rad and a 67% decrease at a rotation angle +0.1 rad. The method is shown to be computationally efficient and numerically stable for grating structures with optimized parameters, and the resulting bottom-grating diffraction efficiencies demonstrate similar trends as those calculated by the 3D finite-difference time-domain simulations. The procedure presented can be directly used in the analysis and design of interlayer waveguide grating coupling for optical interconnects in high-density integrated electronics. © 2016 Optical Society of America

OCIS codes: (050.1950) Diffraction gratings; (050.1960) Diffraction theory; (060.1810) Buffers, couplers, routers, switches, and multiplexers; (130.0130) Integrated optics; (250.5300) Photonic integrated circuits.

https://doi.org/10.1364/AO.55.010006

1. INTRODUCTION

A number of promising optical interconnect solutions have been proposed to achieve compact, high-bandwidth integrated systems. Diffractive optics, e.g., surface-relief gratings, are necessary elements to couple optical signals into (and out of) waveguides on overlaid chips when the integrated system is extended to higher dimensions (2.5D or 3D). However, alignment of diffraction gratings has been a major bottleneck that limits the grating-to-grating coupling efficiency. The need to align the grating couplers and other optical components greatly reduces the possibility of cost-effective manufacturing and automation. Misalignment may result from mechanical and thermal effects which are unavoidable during device handling and operation. As a result, understanding the underlying mechanism and designing misalignment-tolerant grating couplers are important to the fields of packaging and testing.

There are six degrees of freedom to be considered for misalignment analysis, including three lateral (x, y, z) and three

angular (yaw, pitch, roll), where yaw, pitch, and roll are the rotational angles about the z-, y-, and x-axes, respectively. The coordinate system is shown in Fig. 1. For chip-to-chip grating couplers, the lateral displacements of volume holographic gratings [1,2] and surface-relief gratings [3,4] have been experimentally studied. There is limited effort analyzing rotational misalignment, and such efforts all focus on rotations about the y-axis, or equivalently, changes in the incident angle [5,6]. Wu et al. [7] analyzed the yaw, pitch, and roll rotation of a volume grating under vertical incidence (zero incident angle), but they only considered transmission through the grating instead of coupling into a waveguide. Other efforts related to misalignment analysis in the field of optical communication mainly focus on fiber-to-grating coupling [8–11] and laser-to-grating coupling [12]. Misalignment-tolerant structures have been proposed to provide solutions to misalignment problems but those designs did not give general physical insight into the underlying mechanisms [13–15]. Consequently, it is necessary
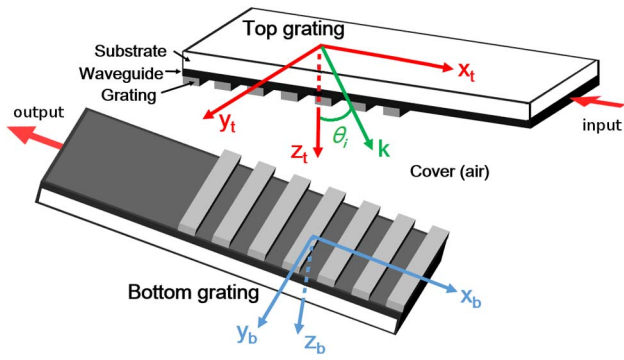
Fig. 1. Schematic representation (not to scale) of the three-dimensional grating-to-grating coupling configuration under angular misalignment.

Fig. 2. Wave vector diagram of the grating (a) in-coupling and (b) out-diffraction process with only 0 and +1 orders. The light in-coupling to the +1 order (a) is the reciprocal process of the guided-wave out-diffracted to the +1 order (b).

to build a comprehensive simulation model for grating-to-grating coupling under angular misalignment.

In the present work, interlayer waveguide grating coupling under angular misalignment is simulated using the 3D rigorous coupled-wave analysis (3D-RCWA) for conical diffraction [16] together with the RCWA equivalent-index-slab (RCWA-EIS) method [17]. The proposed model can handle arbitrary rotations and calculate grating-to-grating coupling efficiency under the pre-defined rotations. The model can also produce the change of bottom-grating diffraction efficiency (or equivalently, the interlayer grating coupling efficiency) as a function of rotation angle about a particular direction. Implemented in MATLAB and providing a simple software scheme, the model is computationally efficient and numerically accurate, compared with the hefty simulation time required for 3D finite-difference time-domain (FDTD) simulations. Given a specific requirement, such as the maximum angular rotation of an interconnect system, the model is capable of optimizing the grating parameters by using the MATLAB optimization toolbox.

2. THEORY AND FORMULATION

The binary rectangular-groove grating considered in this work consists of four layers, namely cover, grating, waveguide, and substrate. The general three-dimensional grating-to-grating coupling configuration is depicted in Fig. 1. The coordinate axes of the top and bottom waveguide gratings are labeled as (x_t, y_t, z_t) and (x_b, y_b, z_b), respectively. A TE-polarized guided wave (with field components E_y, H_z, H_x) of free-space wavelength λ_0 is launched into the top waveguide along the $-x_t$ direction and incident on the top grating. The grating structure is optimized using the method given in [17] such that only the +1-order diffracted light is propagating, as shown in Fig. 2. The +1-order diffracted light from the top grating, whose direction is indicated by the k vector, is then incident conically onto the bottom grating, when the top and bottom gratings are not perfectly aligned. The grating-to-grating coupling efficiency can be approximated by finding the product of the out-diffraction efficiency of the top grating and the in-coupling efficiency of the bottom grating. The following analysis calculates the in-coupling efficiency of the bottom grating under conical incidence. The conical diffraction of a grating structure
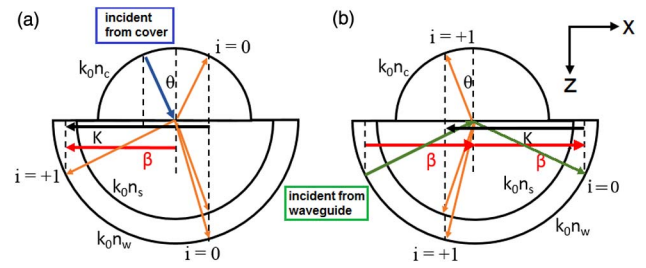
can be analyzed using the RCWA approach [16] if the proper Euler angles (ϕ, θ, ψ) of the z-y'-z'' intrinsic rotation are determined, as show in Fig. 3. A step-by-step analysis is provided in Sections 2.A–2.E.

A. Determination of Rotated Grating Coordinate System

The first step of the misalignment analysis is to determine the coordinate axes of the bottom grating structure, designated as $\hat{x}_b$, $\hat{y}_b$, and $\hat{z}_b$. The coordinate system of the top grating structure, defined by the axes $\hat{x}_t$, $\hat{y}_t$, and $\hat{z}_t$, is set as the reference coordinate system. Since the rotational misalignment is the target of the analysis, the separation between the top and bottom gratings is not emphasized. For simple calculations, both the top and bottom coordinate systems are placed at a common origin and thus no translation is involved. The bottom grating structure is rotated about an arbitrary axis defined by the unit vector $\hat{a}$. As shown in Fig. 4, the rotation of a vector by an angle δ about the axis $\hat{a}$ can be achieved by the following steps:

(1) Rotate the coordinate system about the $\hat{z}_t$-axis such that $\hat{a}$ lies in the $x_t z_t$ plane: $R_z(\theta_1)$.
(2) Rotate the coordinate system about the $\hat{y}_t$-axis such that $\hat{a}$ lies along the z_t-axis: $R_y(\theta_2)$.
(3) Rotate the coordinate system by the desired angle δ about the z_t-axis: $R_z(\delta)$.
(4) Perform the inverse of Step (2): $R_y^{-1}(\theta_2) = R_y(-\theta_2)$.
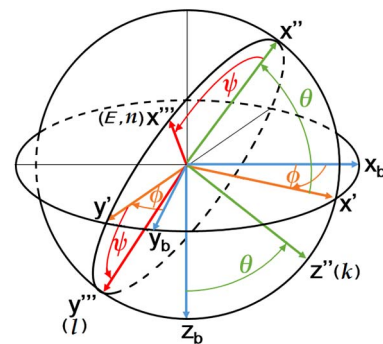(5) Perform the inverse of Step (1): $R_z^{-1}(\theta_1) = R_z(-\theta_1)$,

Fig. 3. Proper Euler angles (ϕ, θ, ψ) for the z-y'-z'' type of intrinsic rotation. The coordinate system first rotates about the z-axis (same as z_b and z') by ϕ, then rotates about the y'-axis (same as y'') by θ, and finally rotates about the z''-axis (same as k and z''') by ψ.
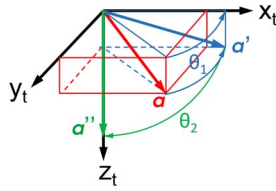
Fig. 4. Rotation about an arbitrary axis $\hat{a}$ can be decomposed into a series of rotation operations. The first step is rotating the vector a about the z_t-axis by an angle θ_1 such that a' is in the $x_t z_t$ plane, and the second step is rotating the vector a' about the y_t-axis by an angle θ_2 such that a'' is along the z-axis. In this figure, both θ_1 and θ_2 are negative (clockwise).

where the rotation matrix $R_z(\gamma)$ is

$$R_z(\gamma) = \begin{bmatrix} \cos\gamma & -\sin\gamma & 0 \\ \sin\gamma & \cos\gamma & 0 \\ 0 & 0 & 1 \end{bmatrix}, \tag{1}$$

if the coordinate system is rotated clockwise (or equivalently, the vector is rotated counterclockwise) by an angle γ about the z-axis, and the rotation matrix $R_y(\beta)$ is

$$R_y(\beta) = \begin{bmatrix} \cos\beta & 0 & \sin\beta \\ 0 & 1 & 0 \\ -\sin\beta & 0 & \cos\beta \end{bmatrix}, \tag{2}$$

if the coordinate system is rotated clockwise by an angle β about the y-axis. As a result, the total operation of rotating about the axis $\hat{a}$ is $R_a = R_z^{-1}(\theta_1)R_y^{-1}(\theta_2)R_z(\delta)R_y(\theta_2)R_z(\theta_1)$, and the bottom coordinate system can be determined as $\hat{x}_b = R_a\hat{x}_t$, $\hat{y}_b = R_a\hat{y}_t$, and $\hat{z}_b = R_a\hat{z}_t$.

B. Determination of Proper Euler Angles

The second step of the misalignment analysis is to determine the proper Euler angles (ϕ, θ, ψ). For a given rotational misalignment configuration, the coordinate axes (x_t, y_t, z_t) and (x_b, y_b, z_b) are known. The bottom coordinate axes are expressed in the top coordinate system. From the system (x_t, y_t, z_t), the system (n, l, k) can be determined as the following unit vectors: $\hat{n} = [0, 1, 0]$, $\hat{l} = [-\cos\theta_i, 0, \sin\theta_i]$, and $\hat{k} = [\sin\theta_i, 0, \cos\theta_i]$, where $\hat{n} = \hat{y}_t = \hat{E}$, $\hat{l} = \hat{k} \times \hat{n}$, and θ_i is the angle between $\hat{k}$ and $\hat{z}_t$ or the incident angle. The direction of the line of nodes, or $\vec{y}'$, is determined by $\vec{y}' = \hat{z}_b \times \hat{k}$. Then ϕ is the angle between $\vec{y}_b$ and $\vec{y}'$, defined as $\phi = \cos^{-1}[\vec{y}_b \cdot \vec{y}'/(|\vec{y}_b||\vec{y}'|)]$; θ is the angle between $\vec{z}_b$ and $\vec{k}$, defined as $\theta = \cos^{-1}[\vec{z}_b \cdot \vec{k}/(|\vec{z}_b||\vec{k}|)]$ (note θ and θ_i are completely different variables); and ψ is the angle between $\hat{l}$ and $\vec{y}'$, defined as $\psi = \cos^{-1}[\hat{l} \cdot \vec{y}'/(|\hat{l}||\vec{y}'|)]$. The above definitions only give the values of the angles. The sign of the angle is defined using the right-hand rule: curl the fingers along the rotation direction, and if the thumb points to the positive direction of the rotation axis, the rotation angle is positive; otherwise, the rotation angle is negative. According to this statement, both θ and ψ are always positive. The sign of ϕ is determined as follows: if the x component of $\hat{y}'$ is larger than the x component of $\hat{y}_b$, ϕ is negative; otherwise, ϕ is positive.

C. Formulations in the System (x, y, z)

After the proper Euler angles (ϕ, θ, ψ) are determined, the conical diffraction problem of the bottom waveguide grating

can be formulated according to [16] with some modifications. The coordinate system (x_b, y_b, z_b) is indicated by (x, y, z) for simplicity, and $z = 0$ is set at the top surface of the grating, as indicated in Fig. 5. The electric and magnetic fields of the cover, grating, waveguide, and substrate layers are expressed as follows:

◊ Electric field in the cover:

$$E_c = E_{inc} + \sum_i (R_{xi}\hat{x} + R_{yi}\hat{y} + R_{zi}\hat{z})$$
$$\times \exp(-jk_{x,i}x - jk_yy + jk_{cz,i}z), \tag{3}$$

where

$$E_{inc} = [(\cos\psi\cos\theta\cos\phi - \sin\psi\sin\phi)\hat{x}$$
$$+ (\cos\psi\cos\theta\sin\phi + \sin\psi\cos\phi)\hat{y} - \cos\psi\sin\theta\hat{z}]$$
$$\cdot \exp[-jk_0n_c(\sin\theta\cos\phi x + \sin\theta\sin\phi y + \cos\theta z)]; \tag{4}$$

◊ Magnetic field in the cover:

$$H_c = H_{inc} + \left(-j\sqrt{\frac{\epsilon_0}{\mu_0}}\right)\sum_i (A_{xi}\hat{x} + A_{yi}\hat{y} + A_{zi}\hat{z})$$
$$\cdot \exp(-jk_{x,i}x - jk_yy + jk_{cz,i}z), \tag{5}$$

where

$$H_{inc} = n_c\sqrt{\frac{\epsilon_0}{\mu_0}}[(-\cos\psi\sin\phi - \sin\psi\cos\phi\cos\theta)\hat{x}$$
$$+ (\cos\psi\cos\phi - \sin\psi\sin\phi\cos\theta)\hat{y} + H_{inc,z}\hat{z}]$$
$$\cdot \exp[-jk_0n_c(\sin\theta\cos\phi x + \sin\theta\sin\phi y + \cos\theta z)]; \tag{6}$$

◊ Electric field in the grating:

$$E_g = \sum_i [S_{xi}(z)\hat{x} + S_{yi}(z)\hat{y} + S_{zi}(z)\hat{z}]\exp(-jk_{x,i}x - jk_yy); \tag{7}$$

◊ Magnetic field in the grating:

$$H_g = \left(-j\sqrt{\frac{\epsilon_0}{\mu_0}}\right)\sum_i [U_{xi}(z)\hat{x} + U_{yi}(z)\hat{y} + U_{zi}(z)\hat{z}]$$
$$\cdot \exp(-jk_{x,i}x - jk_yy); \tag{8}$$

◊ Electric field in the waveguide:

$$E_w = \sum_i [P_{xi}(z)\hat{x} + P_{yi}(z)\hat{y} + P_{zi}(z)\hat{z}]\exp(-jk_{x,i}x - jk_yy); \tag{9}$$
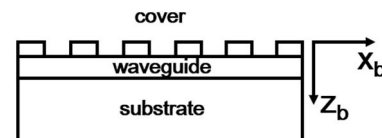

Fig. 5. Coordinate axes of the bottom grating; $z = 0$ is located at the top surface of the grating.

◊ Magnetic field in the waveguide:

$$H_w = \left(-j\sqrt{\frac{\epsilon_0}{\mu_0}}\right)\sum_i [Q_{xi}(z)\hat{x} + Q_{yi}(z)\hat{y} + Q_{zi}(z)\hat{z}]$$
$$\cdot \exp(-jk_{x,i}x - jk_y y); \tag{10}$$

◊ Electric field in the substrate:

$$E_s = \sum_i (T_{xi}\hat{x} + T_{yi}\hat{y} + T_{zi}\hat{z})$$
$$\cdot \exp[-jk_{x,i}x - jk_y y - jk_{sz,i}(z - t_g - t_w)]; \tag{11}$$

◊ Magnetic field in the substrate:

$$H_s = \left(-j\sqrt{\frac{\epsilon_0}{\mu_0}}\right)\sum_i (B_{xi}\hat{x} + B_{yi}\hat{y} + B_{zi}\hat{z})$$
$$\cdot \exp[-jk_{x,i}x - jk_y y - jk_{sz,i}(z - t_g - t_w)], \tag{12}$$

where the summation is from $i = -(s-1)/2$ to $(s-1)/2$ and s is the total number of diffraction orders (an odd number for calculation convenience). The propagation constants $k_{x,i}$, k_y, $k_{cz,i}$, and $k_{sz,i}$ are defined as follows:

◊ Propagation constant in the x direction:

$$k_{x,i} = k_0 n_c \sin\theta \cos\phi - iK, \tag{13}$$

◊ Propagation constant in the y direction:

$$k_y = k_0 n_c \sin\theta \sin\phi, \tag{14}$$

◊ Propagation constant in the z direction:

$$k_{rz,i} = \begin{cases} \sqrt{n_r^2 k_0^2 - k_{x,i}^2 - k_y^2} & n_r^2 k_0^2 > k_{x,i}^2 + k_y^2 \\ -j\sqrt{k_{x,i}^2 + k_y^2 - n_r^2 k_0^2} & n_r^2 k_0^2 < k_{x,i}^2 + k_y^2 \end{cases} \; r = c, s, \tag{15}$$

where $k_0 = 2\pi/\lambda_0$.

The space harmonics of the tangential electric and magnetic fields in the grating are given by [16] as follows:

◊ X component of electric field of ith order in the grating:

$$S_{xi}(z) = \sum_{p=1}^s w_{2,i,p}^g \{C_{2,p}^{g+} \exp[-k_0 q_{2,p}^g(z - z_1)]$$
$$+ C_{2,p}^{g-} \exp[k_0 q_{2,p}^g(z - z_2)]\}, \tag{16}$$

◊ Y component of electric field of ith order in the grating:

$$S_{yi}(z) = \sum_{p=1}^s v_{11,i,p}^g \{C_{1,p}^{g+} \exp[-k_0 q_{2,p}^g(z - z_1)]$$
$$+ C_{1,p}^{g-} \exp[k_0 q_{2,p}^g(z - z_2)]\}$$
$$+ \sum_{p=1}^s v_{12,i,p}^g \{C_{2,p}^{g+} \exp[-k_0 q_{2,p}^g(z - z_1)]$$
$$+ C_{2,p}^{g-} \exp[k_0 q_{2,p}^g(z - z_2)]\}, \tag{17}$$

◊ X component of magnetic field of ith order in the grating:

$$U_{xi}(z) = \sum_{p=1}^s w_{1,i,p}^g \{-C_{1,p}^{g+} \exp[-k_0 q_{2,p}^g(z - z_1)]$$
$$+ C_{2,p}^{g-} \exp[k_0 q_{1,p}^g(z - z_2)]\}, \tag{18}$$

◊ Y component of magnetic field of ith order in the grating:

$$U_{yi}(z) = \sum_{p=1}^s v_{21,i,p}^g \{-C_{1,p}^{g+} \exp[-k_0 q_{2,p}^g(z - z_1)]$$
$$+ C_{1,p}^{g-} \exp[k_0 q_{2,p}^g(z - z_2)]\}$$
$$+ \sum_{p=1}^s v_{22,i,p}^g \{-C_{2,p}^{g+} \exp[-k_0 q_{2,p}^g(z - z_1)]$$
$$+ C_{2,p}^{g-} \exp[k_0 q_{2,p}^g(z - z_2)]\}, \tag{19}$$

where $z_1 = 0$ and $z_2 = t_g$. The space harmonics of the tangential electric and magnetic fields in the waveguide, namely P_{xi}, P_{yi}, Q_{xi}, and Q_{yi}, are of the same forms as Eqs. (16) to (19) except changing the superscript g to w and setting $z_1 = t_g$ and $z_2 = t_g + t_w$. The parameters w, v, and q for the grating layer are defined in [16], while those for the waveguide layer have the same forms as in the grating but can be simplified due to the constant permittivity of the waveguide. In fact, $w_{1,i,p}^w = w_{2,i,p}^w = w_{i,p}^w$ and $q_{1,p}^w = q_{2,p}^w = q_p^w$. Furthermore, given a particular diffraction order i, there exists one and only one $p = \gamma$ such that $w_{i,\gamma}^w = 1$ and $w_{i,p}^w = 0$ for $p \neq \gamma$. As a result, the space harmonics of the tangential electric and magnetic fields in the waveguide can be simplified as follows:

◊ X component of electric field of ith order in the waveguide:

$$P_{xi}(z) = C_{2,\gamma}^{w+} \exp[-k_0 q_\gamma^w(z - t_g)]$$
$$+ C_{2,\gamma}^{w-} \exp[k_0 q_\gamma^w(z - t_g - t_w)], \tag{20}$$

◊ Y component of electric field of ith order in the waveguide:

$$P_{yi}(z) = (v_{11,i,\gamma}^w C_{1,\gamma}^{w+} + v_{12,i,\gamma}^w C_{2,\gamma}^{w+}) \exp[-k_0 q_\gamma^w(z - t_g)]$$
$$+ (v_{11,i,\gamma}^w C_{1,\gamma}^{w-} + v_{12,i,\gamma}^w C_{2,\gamma}^{w-}) \exp[k_0 q_\gamma^w(z - t_g - t_w)]$$
$$= I_i^{w+} \exp[-k_0 q_\gamma^w(z - t_g)] + I_i^{w-} \exp[k_0 q_\gamma^w(z - t_g - t_w)], \tag{21}$$

◊ X component of magnetic field of ith order in the waveguide:

$$Q_{xi}(z) = -C_{1,\gamma}^{w+} \exp[-k_0 q_\gamma^w(z - t_g)]$$
$$+ C_{1,\gamma}^{w-} \exp[k_0 q_\gamma^w(z - t_g - t_w)], \tag{22}$$

◊ Y component of magnetic field of ith order in the waveguide:

$$Q_{yi}(z) = (-v_{21,i,\gamma}^w C_{1,\gamma}^{w+} - v_{22,i,\gamma}^w C_{2,\gamma}^{w+}) \exp[-k_0 q_\gamma^w(z - t_g)]$$
$$+ (v_{21,i,\gamma}^w C_{1,\gamma}^{w-} + v_{22,i,\gamma}^w C_{2,\gamma}^{w-}) \exp[k_0 q_\gamma^w(z - t_g - t_w)]$$
$$= J_i^{w+} \exp[-k_0 q_\gamma^w(z - t_g)] + J_i^{w-} \exp[k_0 q_\gamma^w(z - t_g - t_w)]. \tag{23}$$

Actually, $k_0 q_\gamma^w = jk_{wz,i}$, where $k_{wz,i}$ is defined in the same way as in Eq. (15).

D. Formulations in the System (x', y', z')

Now the coordinate system is switched from (x, y, z) to (x', y', z'), as indicated in Fig. 3. This step simplifies the E field and H field expressions of the incident wave, as can be seen by comparing Eq. (4) and Eq. (6) with Eq. (25) and Eq. (27), respectively. The main goal of switching the coordinate system is to follow the formulation in [16]. The final results will not be affected if the calculations are done in (x, y, z). For a particular diffraction order i, the rotation angle φ_i about the z_b-axis is determined by $\varphi_i = \arctan(k_y/k_{xi})$, and this rotation angle can be visualized in Fig. 6. For the $i = 0$ order, $\varphi_0 = \phi$. The new coordinate system is related to the original system by $x' = \cos\varphi_i X + \sin\varphi_i Y$ and $Y' = -\sin\varphi_i X + \cos\varphi_i Y$, where X and Y represent variables in the original coordinate system, and X' and Y' represent variables in the new coordinate system.

The formulations follow [16] except for those representing the tangential fields in the cover and substrate. Only the modifications are presented here. In the new coordinate system:

◊ Electric field in the cover:

$$E'_c = E'_{\text{inc}} + \sum_i (R'_{xi}\hat{x}' + R'_{yi}\hat{y}' + R_{zi}\hat{z})$$
$$\cdot \exp(-jk'_{x,i}x' - jk'_y y' + jk_{cz,i}z), \qquad (24)$$

where

$$E'_{\text{inc}} = (\cos\psi\cos\theta\hat{x}' + \sin\psi\hat{y}' - \cos\psi\sin\theta\hat{z})$$
$$\cdot \exp[-jk_0 n_c(\sin\theta x' + \cos\theta z)]; \qquad (25)$$

◊ Magnetic field in the cover:

$$H'_c = H'_{\text{inc}} + \left(-j\sqrt{\frac{\epsilon_0}{\mu_0}}\right)\sum_i (A'_{xi}\hat{x}' + A'_{yi}\hat{y}' + A_{zi}\hat{z})$$
$$\cdot \exp(-jk'_{x,i}x' - jk'_y y' + jk_{cz,i}z), \qquad (26)$$

where

$$H'_{\text{inc}} = n_c\sqrt{\frac{\epsilon_0}{\mu_0}}[-\sin\psi\cos\theta\hat{x}' + \cos\psi\hat{y}' + \sin\psi\sin\theta\hat{z}]$$
$$\cdot \exp[-jk_0 n_c(\sin\theta x' + \cos\theta z)]; \qquad (27)$$

◊ Electric field in the substrate:

$$E'_s = \sum_i (T'_{xi}\hat{x}' + T'_{yi}\hat{y}' + T_{zi}\hat{z})$$
$$\cdot \exp[-jk'_{x,i}x' - jk'_y y' - jk_{sz,i}(z - t_g - t_w)]; \qquad (28)$$

◊ Magnetic field in the substrate:

$$H_s = \left(-j\sqrt{\frac{\epsilon_0}{\mu_0}}\right)\sum_i (B'_{xi}\hat{x}' + B'_{yi}\hat{y}' + B_{zi}\hat{z})$$
$$\cdot \exp[-jk'_{x,i}x' - jk'_y y - jk_{sz,i}(z - t_g - t_w)]. \qquad (29)$$

From Maxwell's equations and the characteristics of plane waves $\vec{E} \cdot \vec{k} = 0$, the magnetic field components A'_{xi}, A'_{yi}, B'_{xi}, and B'_{yi} can each be expressed as a function of the electric field components:

$$A'_{xi} = \frac{j}{k_0 k_{c,zi}}[k'_{xi}k'_y R'_{xi} + (k_0^2 n_c^2 - k_{xi}'^2)R'_{yi}], \qquad (30)$$

$$A'_{yi} = \frac{-j}{k_0 k_{c,zi}}[(k_0^2 n_c^2 - k_y'^2)R'_{xi} + k'_{xi}k'_y R'_{yi}], \qquad (31)$$

$$B'_{xi} = \frac{-j}{k_0 k_{s,zi}}[k'_{xi}k'_y T'_{xi} + (k_0^2 n_s^2 - k_{xi}'^2)T'_{yi}], \qquad (32)$$

$$B'_{yi} = \frac{j}{k_0 k_{s,zi}}[(k_0^2 n_s^2 - k_y'^2)T'_{xi} + k'_{xi}k'_y T'_{yi}]. \qquad (33)$$

Then, all the tangential fields in the new coordinate system are matched at boundaries $z = 0$ (cover–grating interface), $z = t_g$ (grating–waveguide interface), and $z = t_g + t_w$ (waveguide–substrate interface), resulting in the following matrices:

◊ At $z = 0$:

$$\begin{bmatrix} \sin\psi\delta_{i0} \\ jn_c\sin\psi\cos\theta\delta_{i0} \\ \cos\psi\cos\theta\delta_{i0} \\ -jn_c\cos\psi\delta_{i0} \end{bmatrix} + \begin{bmatrix} \mathbf{0} & \mathbf{I} \\ -j\mathbf{RA} & -j\mathbf{RB} \\ \mathbf{I} & \mathbf{0} \\ j\mathbf{RC} & j\mathbf{RA} \end{bmatrix}\begin{bmatrix} \mathbf{R}'_x \\ \mathbf{R}'_y \end{bmatrix}$$

$$= \begin{bmatrix} \mathbf{V}^g_{ss} & \mathbf{V}^g_{sp} & \mathbf{V}^g_{ss}\mathbf{X}^g_1 & \mathbf{V}^g_{sp}\mathbf{X}^g_2 \\ \mathbf{W}^g_{ss} & \mathbf{W}^g_{sp} & -\mathbf{W}^g_{ss}\mathbf{X}^g_1 & -\mathbf{W}^g_{sp}\mathbf{X}^g_2 \\ \mathbf{V}^g_{ps} & \mathbf{V}^g_{pp} & \mathbf{V}^g_{ps}\mathbf{X}^g_1 & \mathbf{V}^g_{pp}\mathbf{X}^g_2 \\ \mathbf{W}^g_{ps} & \mathbf{W}^g_{pp} & -\mathbf{W}^g_{ps}\mathbf{X}^g_1 & -\mathbf{W}^g_{pp}\mathbf{X}^g_2 \end{bmatrix}\begin{bmatrix} \mathbf{C}^{g+}_1 \\ \mathbf{C}^{g+}_2 \\ \mathbf{C}^{g-}_1 \\ \mathbf{C}^{g-}_2 \end{bmatrix}; \qquad (34)$$

◊ At $z = t_g$:

$$\begin{bmatrix} \mathbf{V}^g_{ss}\mathbf{X}^g_1 & \mathbf{V}^g_{sp}\mathbf{X}^g_2 & \mathbf{V}^g_{ss} & \mathbf{V}^g_{sp} \\ \mathbf{W}^g_{ss}\mathbf{X}^g_1 & \mathbf{W}^g_{sp}\mathbf{X}^g_2 & -\mathbf{W}^g_{ss} & -\mathbf{W}^g_{sp} \\ \mathbf{V}^g_{ps}\mathbf{X}^g_1 & \mathbf{V}^g_{pp}\mathbf{X}^g_2 & \mathbf{V}^g_{ps} & \mathbf{V}^g_{pp} \\ \mathbf{W}^g_{ps}\mathbf{X}^g_1 & \mathbf{W}^g_{pp}\mathbf{X}^g_2 & -\mathbf{W}^g_{ps} & -\mathbf{W}^g_{pp} \end{bmatrix}\begin{bmatrix} \mathbf{C}^{g+}_1 \\ \mathbf{C}^{g+}_2 \\ \mathbf{C}^{g-}_1 \\ \mathbf{C}^{g-}_2 \end{bmatrix}$$

$$= \begin{bmatrix} \mathbf{V}^w_{ss} & \mathbf{V}^w_{sp} & \mathbf{V}^w_{ss}\mathbf{X}^w_1 & \mathbf{V}^w_{sp}\mathbf{X}^w_2 \\ \mathbf{W}^w_{ss} & \mathbf{W}^w_{sp} & -\mathbf{W}^w_{ss}\mathbf{X}^w_1 & -\mathbf{W}^w_{sp}\mathbf{X}^w_2 \\ \mathbf{V}^w_{ps} & \mathbf{V}^w_{pp} & \mathbf{V}^w_{ps}\mathbf{X}^w_1 & \mathbf{V}^w_{pp}\mathbf{X}^w_2 \\ \mathbf{W}^w_{ps} & \mathbf{W}^w_{pp} & -\mathbf{W}^w_{ps}\mathbf{X}^w_1 & -\mathbf{W}^w_{pp}\mathbf{X}^w_2 \end{bmatrix}\begin{bmatrix} \mathbf{C}^{w+}_1 \\ \mathbf{C}^{w+}_2 \\ \mathbf{C}^{w-}_1 \\ \mathbf{C}^{w-}_2 \end{bmatrix}; \qquad (35)$$
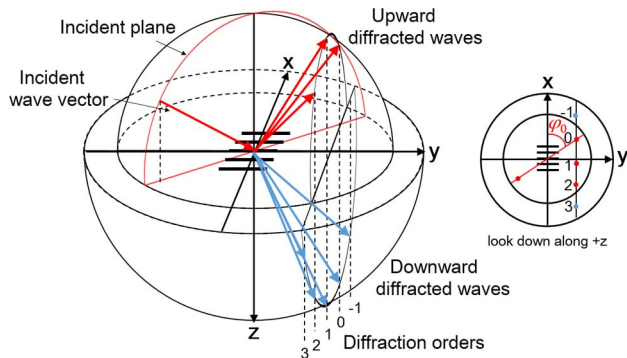

Fig. 6. 3D wave vector diagram of conical diffraction. The top half sphere represents the $k_0 n_c$ surface, and the bottom half sphere represents the $k_0 n_s$ surface.

◊ At $z = t_g + t_w$:

$$\begin{bmatrix} \mathbf{V}_{ss}^w\mathbf{X}_1^w & \mathbf{V}_{sp}^w\mathbf{X}_2^w & \mathbf{V}_{ss}^w & \mathbf{V}_{sp}^w \\ \mathbf{W}_{ss}^w\mathbf{X}_1^w & \mathbf{W}_{sp}^w\mathbf{X}_2^w & -\mathbf{W}_{ss}^w & -\mathbf{W}_{sp}^w \\ \mathbf{V}_{ps}^w\mathbf{X}_1^w & \mathbf{V}_{pp}^w\mathbf{X}_2^w & \mathbf{V}_{ps}^w & \mathbf{V}_{pp}^w \\ \mathbf{W}_{ps}^w\mathbf{X}_1^w & \mathbf{W}_{pp}^w\mathbf{X}_2^w & -\mathbf{W}_{ps}^w & -\mathbf{W}_{pp}^w \end{bmatrix} \begin{bmatrix} \mathbf{C}_1^{w+} \\ \mathbf{C}_2^{w+} \\ \mathbf{C}_1^{w-} \\ \mathbf{C}_2^{w-} \end{bmatrix}$$

$$= \begin{bmatrix} \mathbf{0} & \mathbf{I} \\ j\mathbf{TA} & j\mathbf{TB} \\ \mathbf{I} & \mathbf{0} \\ -j\mathbf{TC} & -j\mathbf{TA} \end{bmatrix} \begin{bmatrix} \mathbf{T}_x' \\ \mathbf{T}_y' \end{bmatrix}, \tag{36}$$

where

$$\mathbf{V}_{ss}^r = \mathbf{F}_c\mathbf{V}_{11}^r, \qquad \mathbf{V}_{sp}^r = -\mathbf{F}_s\mathbf{W}_2^r + \mathbf{F}_c\mathbf{V}_{12}^r,$$

$$\mathbf{W}_{ss}^r = \mathbf{F}_c\mathbf{W}_1^r + \mathbf{F}_s\mathbf{V}_{21}^r, \qquad \mathbf{W}_{sp}^r = \mathbf{F}_s\mathbf{V}_{22}^r,$$

$$\mathbf{V}_{ps}^r = \mathbf{F}_s\mathbf{V}_{11}^r, \qquad \mathbf{V}_{pp}^r = \mathbf{F}_c\mathbf{W}_2^r + \mathbf{F}_s\mathbf{V}_{12}^r,$$

$$\mathbf{W}_{ps}^r = -\mathbf{F}_s\mathbf{W}_1^r + \mathbf{F}_c\mathbf{V}_{21}^r, \qquad \mathbf{W}_{sp}^r = \mathbf{F}_s\mathbf{V}_{22}^r, \tag{37}$$

where $r = g$ or w, $\mathbf{F}_c$, $\mathbf{F}_s$, $\mathbf{RA}$, $\mathbf{RB}$, $\mathbf{RC}$, $\mathbf{TA}$, $\mathbf{TB}$, and $\mathbf{TC}$ are diagonal matrices with diagonal elements $\cos\varphi_i$, $\sin\varphi_i$, $k'_{xi}k'_y/(k_0k_{c,zi})$, $(k_0^2n_c^2 - k'^2_{xi})/(k_0k_{c,zi})$, $(k_0^2n_c^2 - k'^2_y)/(k_0k_{c,zi})$, $k'_{xi}k'_y/(k_0k_{s,zi})$, $(k_0^2n_s^2 - k'^2_{xi})/(k_0k_{s,zi})$, $(k_0^2n_s^2 - k'^2_y)/(k_0k_{s,zi})$, respectively, and the matrices $\mathbf{W}^r$, $\mathbf{V}^r$ consist of elements w and v as defined in [16]. Note the field amplitudes in the grating region correspond to the (x_t, y_t, z_t) coordinate system. After solving the above matrix equations using the transfer matrix approach [18] or singular value decomposition [17], the field amplitudes R, T, and C can be determined. The diffraction efficiencies in the cover (DE_c) and the substrate (DE_s) can be subsequently calculated:

$$DE_{c,i} = \frac{\mathrm{Re}[R'_{xi}(-jA'_{yi})^* - R'_{yi}(-jA'_{xi})^*]}{n_c\cos\theta}, \tag{38}$$

$$DE_{s,i} = \frac{\mathrm{Re}[T'_{xi}(-jB'_{yi})^* - T'_{yi}(-jB'_{xi})^*]}{n_c\cos\theta}. \tag{39}$$

The above formulations produce the same results as those presented in [16]. The sum of the diffraction efficiencies is unity as a result of energy conservation in the z direction. Compared with those presented in [16], the present formulations have the advantages that the x and y components of the electric and magnetic fields are clearly presented and calculated, and they can be easily referenced in the following analysis.

E. Determination of Coupling Efficiency into the Waveguide

When the RCWA-based approach is used, the coupling efficiency into the waveguide can only be determined from the out-diffraction process, taking advantage of the light reciprocity. This is because the conservation of energy is only fulfilled in the normal direction of the waveguide plane (z direction), and there is no direct comparison between the incident light power and the guided power in the waveguide. The EIS method [17] was proposed to determine the radiation factor α of an arbitrary waveguide grating for TE polarization, which could be subsequently used to calculate the single-grating out-diffraction efficiency and approximate grating-to-grating coupling efficiency. The EIS method can also be used to analyze the

coupling efficiency under conical mounting, provided the propagating 0 and +1 orders are dominant.

Under perfect grating-to-grating alignment, a TE-polarized guided wave (with field components E_y, H_z, H_x) with propagation constant β is diffracted out of the top grating in the direction of $i = +1$ order and incident onto the bottom grating. As a result, the propagation constant of the coupled wave in the bottom waveguide should also be β. When the bottom grating is rotated relative to the top grating, the out-diffracted light from the top grating is conically incident on the bottom grating. For demonstration purposes, only coupling into the TE mode of the bottom grating is considered.

The first step in determining the coupling efficiency into the bottom waveguide is to find the equivalent index slabs with indices n_l that reproduce the fields outside of the grating layer. All fields in the structures as well as the propagation constants can be readily obtained from the in-coupling process discussed in the previous sections. Four equivalent index layers with uniform refractive indices are used to replace the grating layer, and the ith order electric field in the y direction of the lth slab is

$$E_{ly,i}(z) = C_i^{l+}\exp\{-jk_{lz,i}[z - (l-1)t_l]\}$$
$$+ C_i^{l-}\exp[jk_{lz,i}(z - lt_l)], \tag{40}$$

where $t_l = t_g/4$. With small rotation angles, higher diffraction orders may propagate but they are not dominant. Therefore, only two diffraction orders (0 and +1) will be considered in determining the equivalent indices. By imposing boundary conditions on the tangential electric (E_y) and magnetic (H_x) fields in the coordinate system (x_b, y_b, z_b), the following transfer matrix formulation can be obtained for the $i = 0$ and +1 orders:

$$\begin{bmatrix} a\delta_{i0} + R_{yi} \\ b\delta_{i0} - jk_0A_{xi} \end{bmatrix} = \prod_{l=1}^4 \begin{bmatrix} 1 & X_{l,i} \\ -\tilde{k}_{lz,i} & \tilde{k}_{lz,i}X_{l,i} \end{bmatrix} \begin{bmatrix} X_{l,i} & 1 \\ -\tilde{k}_{lz,i}X_{l,i} & \tilde{k}_{lz,i} \end{bmatrix}^{-1}$$
$$\times \begin{bmatrix} I_i^{w+} + I_i^{w-}X_{w,i} \\ -jk_0(-C_{i,\gamma}^{w+} + C_{i,\gamma}^{w-}X_{w,i}) \end{bmatrix}, \tag{41}$$

where $X_{l,i} = \exp(-j\tilde{k}_{lz,i}t_l)$, $X_{w,i} = \exp(-jk_{wz,i}t_w)$, $a = \cos\psi\cos\theta\sin\phi + \sin\psi\cos\phi$, $b = -k_0n_c(\cos\psi\sin\phi + \sin\psi\cos\phi\cos\theta)$, $R_{yi} = \sin\varphi_iR'_{xi} + \cos\varphi_iR'_{yi}$, $A_{xi} = \cos\varphi_iA'_{xi} - \sin\varphi_iA'_{yi}$, and $\tilde{k}_{lz,i}$ is defined as

$$\tilde{k}_{lz,i} = \begin{cases} \sqrt{n_l^2k_0^2 - k_{x,i}^2} & \mathrm{Re}(\tilde{k}_{lz,i}) > \mathrm{Im}(\tilde{k}_{lz,i}) \\ -\sqrt{n_l^2k_0^2 - k_{x,i}^2} & \mathrm{Re}(\tilde{k}_{lz,i}) < \mathrm{Im}(\tilde{k}_{lz,i}) \end{cases}, \tag{42}$$

because the unknowns n_l are complex-valued.

Equation (41) generates two equations for each of the $i = 0$ and +1 orders, and thus there will be a total of four equations. The problem then becomes finding four equivalent refractive indices n_l such that the four equations are satisfied simultaneously. This is achieved with the MATLAB function *fsolve* with the Trust-Region–Dogleg algorithm [19].

After the equivalent indices are determined, the radiation factor α is the single unknown, which is incorporated in the following transfer matrix formulation:

$$
\begin{bmatrix} 1 \\ \tilde{k}_{cz,i} \end{bmatrix} R_i = \prod_{l=1}^{4} \begin{bmatrix} 1 & X_{l,i} \\ -\tilde{k}_{lz,i} & \tilde{k}_{lz,i} X_{l,i} \end{bmatrix} \begin{bmatrix} X_{l,i} & 1 \\ -\tilde{k}_{lz,i} X_{l,i} & \tilde{k}_{lz,i} \end{bmatrix}^{-1}
$$

$$
\times \begin{bmatrix} 1 & X_{w,i} \\ -\tilde{k}_{wz,i} & \tilde{k}_{wz,i} X_{w,i} \end{bmatrix} \begin{bmatrix} X_{w,i} & 1 \\ -\tilde{k}_{wz,i} X_{w,i} & \tilde{k}_{wz,i} \end{bmatrix}^{-1}
$$

$$
\times \begin{bmatrix} 1 \\ -\tilde{k}_{sz,i} \end{bmatrix} T_i = \begin{bmatrix} Q_{i,1} \\ Q_{i,2} \end{bmatrix} T_i, \tag{43}
$$

valid for both $i = 0$ and $+1$ orders, where $\tilde{k}_{cz,i}$, $\tilde{k}_{wz,i}$, $\tilde{k}_{sz,i}$ are calculated based on Eq. (42), in which $k_{x,0} = \beta - j\alpha$ and $k_{x,1} = K - \beta - j\alpha$, where K is the grating vector ($K = 2\pi/\Lambda$, Λ is the grating period). The sign of the real part of $k_{x,1}$ is not of consequence since $k_{x,1}$ is squared when calculating propagation constants in the z direction. Equation (43) results in two equations $\tilde{k}_{cz,i} Q_{i,1} = Q_{i,2}$ ($i = 0$ or 1) with one unknown α, which can be solved by MATLAB function *fsolve* with the Levenberg–Marquardt algorithm.

After α is determined, the diffraction efficiency can be calculated using the method stated in [17], except changing the expression for $k_{x,i}$ from Eq. (7) of [17] to $k_{x,i} = k_0 n_c \sin\theta \cos\phi - iK$ when calculating the matrices involved in Eq. (23) of [17].

3. RESULTS AND DISCUSSION

A. System under Investigation

For demonstration purposes, two optimized binary grating designs obtained by the RCWA-EIS method [17] are used to investigate the rotation effects on grating-to-grating coupling efficiency. The given parameters are as follows: free-space wavelength $\lambda_0 = 1.55$ μm, cover refractive index $n_c = 1$ (air), substrate refractive index $n_s = 1.45$ (SiO$_2$), grating groove refractive index $n_{gr} = 1$ (air), grating ridge refractive index $n_{rd} = 2.46$ (Si$_3$N$_4$), waveguide refractive index $n_w = 3.45$ (Si), grating fill factor $f = 0.5$, number of grating periods $N = 30$ or 50 (depending on the rotation configuration), waveguide thickness $t_w = 0.22$ μm, and waveguide separation in the z direction $d = 2$ μm. The fundamental mode propagation constant of the 0.22 μm thick waveguide is calculated to be $\beta_0 = 11.3710$ μm^{-1}. The total number of space harmonics is set to be $n = 7$. Under the perfectly aligned condition, the coupling angle θ, grating period Λ, grating thickness t_g, preferential coupling ratio (PC), radiation factor (α), single-grating diffraction efficiency (DE) at $N = 30$ and $N = 50$ of two optimized cases are summarized in Table 1. The grating structures are optimized using the method presented in [17]. Randomly selecting grating parameters may cause irregular and unstable results, which cannot correctly represent changes and trends in diffraction efficiencies. Each case will be investigated in the situation for which the bottom substrate is rotated about the x_t-axis, z_t-axis, and the vector [2 2 1], respectively.

For all the analyses presented in this work, the coupling efficiency into the TE mode (with field components E_y, H_z, H_x) is calculated.

The grating-to-grating coupling efficiency η can be approximated by $\eta = \text{DE}_t \cdot \text{DE}_b$, where DE_t and DE_b are the single-grating diffraction efficiencies of the top and the bottom grating, respectively. Since the misalignment is treated as the relative rotation of the bottom grating with respect to the top grating, the top-grating diffraction efficiency is the same as that in the perfectly aligned situation; that is, $\text{DE}_t = \sqrt{\eta_0}$, where η_0 is the grating-to-grating coupling efficiency under perfect alignment. Thus, the bottom-grating diffraction efficiency can be approximated as $\text{DE}_b = \eta/\sqrt{\eta_0}$. This approximation is used to obtain the bottom-grating diffraction efficiency from the grating-to-grating coupling efficiency calculated by 3D-FDTD. The RCWA-EIS calculations consider coupling the out-diffracted light from the top grating into the TE mode of the bottom waveguide. The 3D-FDTD simulations calculate the total guided flux (both TE and TM contributions) in the bottom grating, but the TM contributions are smaller than the TE ones, as discussed in the following section.

B. Rotation about the x_t-Axis

Figures 7(a) and 7(b) show the preferential coupling ratios (PC-EIS) or the branching ratio calculated by the RCWA-EIS method, the bottom-grating diffraction efficiencies calculated by the RCWA-EIS method (DE-EIS) and 3D-FDTD simulation (DE-FDTD) for the two cases when the bottom grating is rotated about the x_t-axis. Figures 7(c) and 7(d) show the radiation factor α for the two cases. It can be observed that PC exhibits negligible changes as the rotation angle about the x_t-axis changes from −0.1 rad (−5.73°) to 0.1 rad (5.73°). This indicates that for an infinitely long and infinitely wide grating, the in-coupled light of TE polarization is unaffected when the rotation angle is small (±5.73°). This is due to the fact that the Bragg condition is not significantly disturbed when the grating is rotated about the x_t- (x_b- equivalently) axis, which is perpendicular to the groove line. It can also be observed that the shape of the DE-EIS curves is largely determined by the shape of the α curves, which means the radiation is a critical factor in determining the bottom-grating diffraction efficiency when the grating length $\ell = N \cdot \Lambda$ is limited in this rotation configuration. The radiation factor smoothly increases as the rotation angle increases from the perfectly aligned situation ($\alpha = 0.0138$ for Case 1 and $\alpha = 0.0167$ for Case 2 at rotation angle $= 0$), giving rise to a valley-shaped DE-EIS curve. At rotation angle ±0.1 rad (±5.73°), the DE-EIS increases about 10% for Case 1 and 5% for Case 2. The increase in diffraction efficiency is well known in over-modulated gratings under off-Bragg conditions [20]. The FDTD results also demonstrate the trend in which diffraction efficiency increases

Table 1.   Optimized Parameters and Calculated Single-Grating Diffraction Efficiencies for Binary Grating Cases 1 and 2

Case Number	θ_i rad (deg)	Λ μm	t_g μm	PC	α μm^{-1}	DE $N = 50$	DE at $N = 30$
1	0.2665 rad (15.27°)	0.6316	0.3951	0.7734	0.0138	0.4499	0.3150
2	0.2021 rad (11.58°)	0.6477	0.3249	0.7163	0.0167	0.4735	0.3420

as rotation angle about the x_t-axis increases. The 3D-FDTD calculates the total guided flux in the bottom waveguide along the x_b direction defined by the following equation:

$$\bar{S} \cdot \hat{x}_b = \frac{1}{2} \text{Re}(E_y \cdot H_z^* - E_z \cdot H_y^*), \qquad (44)$$

where the first part is the TE contribution and the second part is the TM contribution. However, the TM power is much smaller, as shown in Fig. 8. As a result, the flux calculated by 3D-FDTD can be treated as TE-type. An important observation should be made regarding the numerical instability of the 3D-FDTD calculation, and this is discussed in Appendix A.

It generally requires 3 days to finish one 3D-FDTD simulation at a resolution of 60 ppd (pixels per unit distance) with 20-core parallel computing, and it would take even longer when the resolution is set to a higher value. In comparison, it takes less than 1 min for the RCWA-EIS method to generate the entire curves shown in Fig. 7.

C. Rotation about the z_t-Axis

Figures 9(a) and 9(b) show the PC-EIS, DE-EIS, and DE-FDTD plots for the two cases when the bottom grating is rotated about the z_t-axis. Figures 9(c) and 9(d) show the α plots for the two cases. The α curve for Case 1 exhibits a noticeably wavy shape due to numerical sensitivity problems in the RCWA-EIS method. In order to give a better presentation, the curve is Gaussian-fitted. The same fitting procedure is also done on the α curve for Case 2. Like in the x-rotation cases, the PC curves exhibit negligible changes as the bottom grating rotates about the z_t-axis, and the shape of the DE-EIS curves is determined by those of the radiation factors. At rotation angle ± 0.1 rad ($\pm 5.73°$), the DE-EIS decreases about 25% for both cases. The FDTD results are in good agreement with the RCWA-EIS ones, because rotating about the z_t-axis, or equivalently, the surface normal of the waveguide, does not suffer from the staircase problem. In other words, the waveguide surface remains flat, and the only place that requires the staircase approximation is on the edges. Since the width of the waveguide ($W = 10$ μm) is set much larger than the

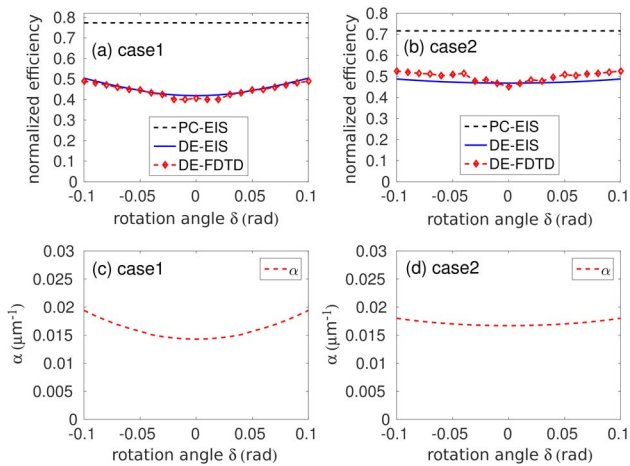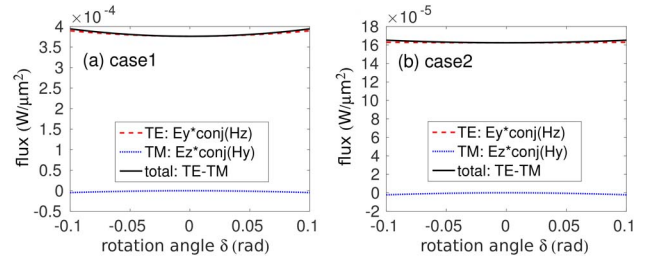**Fig. 8.** Guided power along the x_b direction in the bottom waveguide, including TE power, TM power and total power, calculated by RCWA. Power is integrated from $z = t_g$ to $z = t_g + t_w$ for a unit length in the y_b direction.
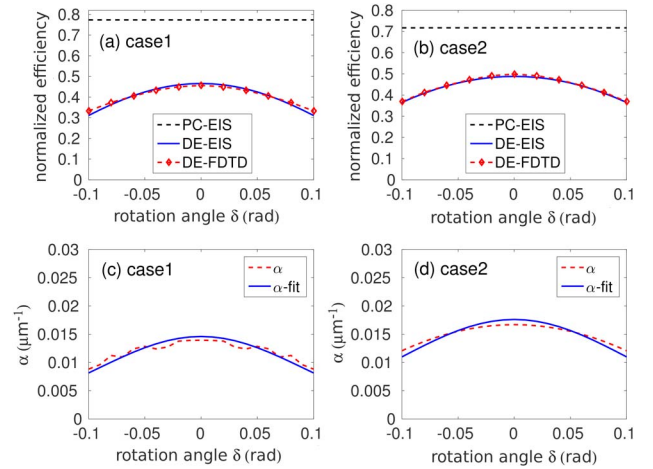
Fig. 9. Plots of PC-EIS, DE-EIS, DE-FDTD, and α for Cases 1 and 2, respectively, when the bottom system is rotated about the z_t-axis. The number of grating periods N is set to 50.

waveguide thickness ($t_g = 0.22$ μm) to model a slab waveguide, the rough edges would not affect the field distribution in the slab structure.

D. Rotation about the Vector [2 2 1]

Figures 10(a) and 10(b) show the PC-EIS, DE-EIS, and DE-FDTD plots for the two cases when the bottom grating is rotated about an axis defined by the vector [2 2 1] in the top coordinate system. Figures 10(c) and 10(d) show the α plots for the two cases. Since the bottom waveguide may be in contact with the top waveguide after rotations in FDTD models, a shorter grating length with $N = 30$ is used instead of $N = 50$. The location of the corners of the waveguides and grating ridges are calculated to ensure the top and bottom structures are not in contact. In this rotation configuration, α changes significantly and it influences the definition of DE-EIS. The resulting shape of the DE-EIS curves is not symmetric. The rotation axis has a y_t component, and rotating about the y_t-axis has an equivalent effect as changing the incident angle of the incoming light to the bottom grating, which greatly disturbs the Bragg condition and induces a large change in the diffraction efficiency. Both the DE-EIS and DE-FDTD curves first increase and then decrease when the rotation angle changes from 0 to −0.1 rad (−5.73°), while the
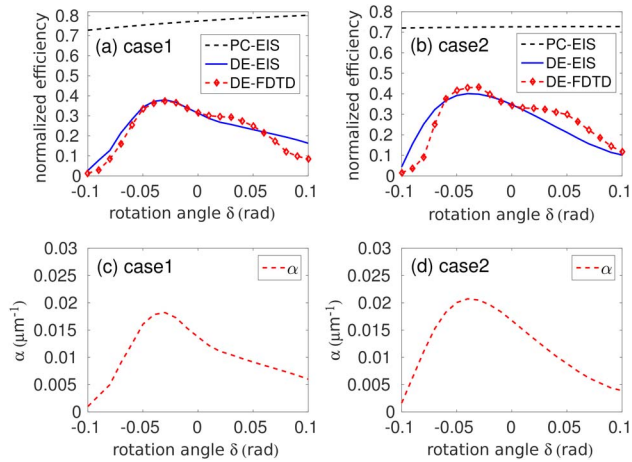
Fig. 7. Plots of PC-EIS, DE-EIS, DE-FDTD, and α for Cases 1 and 2, respectively, when the bottom system is rotated about the x_t-axis. The number of grating periods N is set to 50.

Fig. 10. Plots of PC-EIS, DE-EIS, DE-FDTD, and α for Cases 1 and 2, respectively, when the bottom system is rotated about the vector [2 2 1]. The number of grating periods N is set to 30.

curves monotonically decrease when the rotation angle changes from 0 to 0.1 rad (5.73°).

While the data points of DE-EIS and DE-FDTD at 0 rad rotation match well, the general shape of the curves at the two ends exhibits a noticeable discrepancy. This is because an infinite-long slab waveguide grating is assumed in the RCWA-EIS method, while structures with limited dimensions are modeled in the FDTD simulation. The influence of this geometric factor is explained using Fig. 11. The input light is launched into the top waveguide along the $-x$ direction and out-diffracted when it is incident onto the top grating. Both the out-diffracted power and the guided power in the top waveguide exhibit an exponential decay along the $-x$ direction. When the bottom waveguide is rotated by $+\delta$ about the y-axis, the right end of the bottom waveguide is closer to the top waveguide, and the high power (indicated by the thickest arrow) confined in the top waveguide may be evanescent-coupled to the bottom waveguide, resulting in larger diffraction efficiencies at positive rotation angles. On the contrary, the left end of the bottom waveguide is closer to the top grating when the bottom grating is rotated by $-\delta$. Since the power at the left end is much smaller, the coupled power in the bottom waveguide is negligible. The same reasoning can be made in explaining the offsets of the DE curves obtained by RCWA and FDTD in Fig. 10. As shown in Fig. 12, the positively rotated grating is closer to the high-power end of the top grating, resulting in a moderate efficiency hill of DE-FDTD in the $\delta > 0$ region, while the negatively rotated bottom grating is closer to
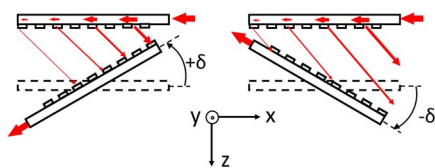

Fig. 11. Schematic diagram show positive ($+\delta$) and negative ($-\delta$) rotation of the bottom grating about the y-axis. Rotation angles are exaggerated.
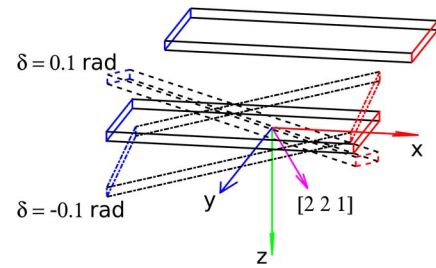

Fig. 12. MATLAB-generated figure shows the rotation of the bottom grating about the vector [2 2 1]. The geometries defined by the solid lines represent the unrotated top and bottom gratings. The geometries defined by the dashed lines and dashed-dotted lines represent the bottom grating rotated 0.1 rad and –0.1 rad about [2 2 1], respectively.

the low-power end of the top grating, resulting in lower efficiency in the $\delta < 0$ region.

4. CONCLUSIONS

In this work, angular (rotational) misalignment of overlaid waveguide gratings was analyzed using the 3D-RCWA method together with the RCWA-EIS method. The RCWA-EIS method has been used to calculate and optimize single-grating diffraction efficiencies under perfect alignment. In the present work, it has been extended to the conical diffraction cases and applied to the simulation of waveguide-grating-to-waveguide-grating coupling efficiency under angular misalignment. The method is computationally efficient and generally accurate compared with the 3D-FDTD simulation. In one example, the computational time of an interlayer grating coupler model was reduced from 3 days to less than 1 min by using RCWA-EIS instead of FDTD with minimal error. This work offers a feasible simulation tool for the analysis and design of interlayer waveguide grating coupling for optical interconnects in high-density electronics.

APPENDIX A: ACCURACY OF FDTD CALCULATION

The accuracy of the 3D-FDTD calculation is largely determined by the resolution, or number of pixels (grids) per unit distance (this unit will be given as "ppd" in the following discussion). The 3D-FDTD is based on a set of cubic grids, which cannot properly represent a slanted surface; instead, a staircase substitution is necessary to model the rotated 3D geometry. This requires relatively high resolution to calculate correctly the fields and fluxes. For example, in Fig. 13, finer grids result
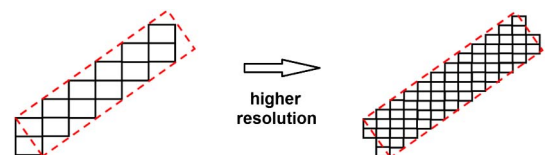

Fig. 13. In the 2D-FDTD simulation, the whole computation cell is populated by rectangular grids (or cubic grids for 3D). A slanted rectangle (represented by the area circled by the red dashed line) is modeled as a cluster of grids. The slanted surface is rougher when the resolution (number of grids per unit length) is smaller.
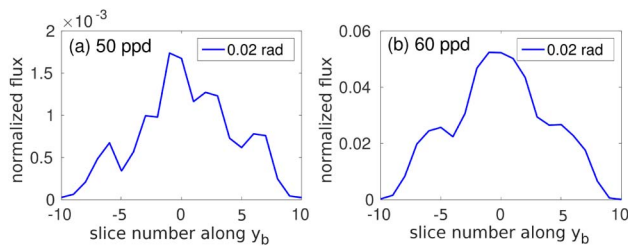
Fig. 14. Guided flux confined in the waveguide cross section for Case 2 with rotation angle 0.02 rad. Left: resolution is 50 ppd; right: resolution is 60 ppd. Flux data were obtained from the MEEP FDTD simulation in which dimensionless (or relative) units are assumed in all calculations.
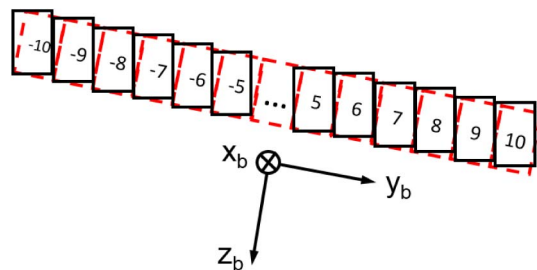

Fig. 15. Cross section of the waveguide is equally divided into 21 sections, which are labeled from -10 to 10 along the y_b direction.

in a smoother surface compared with coarser grids. If the resolution is not properly set, the FDTD simulation result will be invalid. Figure 14 compares the flux in the waveguide calculated by FDTD at resolutions 50 ppd and 60 ppd, respectively, when the bottom system of Case 2 is rotated 0.02 rad about the x_t-axis. The slice number is defined in Fig. 15. It is observed that the flux calculated at resolution 50 ppd is on the order of 1×10^{-3} units, which is 1 order of magnitude smaller than the fluxes calculated at resolution 60 ppd. This indicates that 50 ppd is not large enough to model correctly the waveguide fields; that is, the waveguide surface is too rough to guide a wave and the rough edges may serve as scattering centers. In fact, the total guided flux calculated by the FDTD simulation would be different but would converge to the same order of magnitude when the resolution is set at different values, which is a conclusion drawn after the simulations at resolutions 60, 70, and 80 ppd were performed.

REFERENCES

1. M. Cabezón, I. Garcés, A. Villafranca, J. Pozo, P. Kumar, and A. Kaźmierczak, "Silicon-on-insulator chip-to-chip coupling via out-of-plane or vertical grating couplers," Appl. Opt. **51**, 8090–8094 (2012).
2. S. K. Patra, J. Ma, V. H. Ozguz, and S. H. Lee, "Alignment issues in packaging for free-space optical interconnects," Opt. Eng. **33**, 1561–1570 (1994).
3. S. Bernabé, C. Kopp, M. Volpert, J. Harduin, J.-M. Fédéli, and H. Ribot, "Chip-to-chip optical interconnections between stacked self-aligned SOI photonic chips," Opt. Express **20**, 7886–7894 (2012).
4. J. Yao, X. Zheng, G. Li, I. Shubin, H. Thacker, Y. Luo, K. Raj, J. E. Cunningham, and A. V. Krishnamoorthy, "Grating-coupler based low-loss optical interlayer coupling," in *8th IEEE International Conference on Group IV Photonics* (IEEE, 2011), pp. 383–385.
5. A. V. Mulé, R. Villalaz, T. K. Gaylord, and J. D. Meindl, "Quasi-free-space optical coupling between diffraction grating couplers fabricated on independent substrates," Appl. Opt. **43**, 5468–5475 (2004).
6. G. S. Chan, M. Li, and S. J. Sheard, "Grating-assisted waveguide chip-to-chip interconnects," Proc. SPIE **2213**, 267–277 (1994).
7. S.-D. Wu, T. K. Gaylord, E. N. Glytsis, and Y.-M. Wu, "Angular sensitivities of volume gratings for substrate-mode optical interconnects," Appl. Opt. **44**, 4447–4453 (2005).
8. D. Taillaert, F. Van Laere, M. Ayre, W. Bogaerts, D. Van Thourhout, P. Bienstman, and R. Baets, "Grating couplers for coupling between optical fibers and nanophotonic waveguides," Jpn. J. Appl. Phys. **45**, 6071–6077 (2006).
9. D. T. Neilson, "Tolerance of optical interconnections to misalignment," Appl. Opt. **38**, 2282–2290 (1999).
10. R. Zhang and F. G. Shi, "Novel fiber optic alignment strategy using Hamiltonian algorithm and Matlab/Simulink," Opt. Eng. **42**, 2240–2245 (2003).
11. Z. Tang, R. Zhang, S. Mondal, and F. Shi, "Fiber-optic alignment automation: tolerance analysis in coupling with a wedged single mode fiber," Opt. Commun. **199**, 95–101 (2001).
12. S. Romero-García, B. Marzban, S. S. Azadeh, F. Merget, B. Shen, and J. Witzens, "Misalignment tolerant couplers for hybrid integration of semiconductor lasers with silicon photonics parallel transmitters," Proc. SPIE **9133**, 91331A (2014).
13. S. Romero-García, B. Shen, F. Merget, B. Marzban, and J. Witzens, "Alignment tolerant couplers for silicon photonics," IEEE J. Sel. Top. Quantum Electron. **21**, 765–778 (2015).
14. Z. Zhang, B. Huang, Z. Zhang, H. Liu, H. Li, and H. Chen, "Misalignment-tolerant silicon optical modulator with surface-normal optical interface," IEEE Photon. Technol. Lett. **27**, 1052–1055 (2015).
15. H. Yamada, M. Nozawa, M. Kinoshita, and K. Ohashi, "Vertical-coupling optical interface for on-chip optical interconnection," Opt. Express **19**, 698–703 (2011).
16. M. G. Moharam, E. B. Grann, D. A. Pommet, and T. K. Gaylord, "Formulation for stable and efficient implementation of the rigorous coupled-wave analysis of binary gratings," J. Opt. Soc. Am. A **12**, 1068–1076 (1995).
17. C. Wan, T. K. Gaylord, and M. S. Bakir, "Grating design for interlayer optical interconnection of in-plane waveguides," Appl. Opt. **55**, 2601–2610 (2016).
18. M. G. Moharam, D. A. Pommet, E. B. Grann, and T. K. Gaylord, "Stable implementation of the rigorous coupled-wave analysis for surface-relief gratings: enhanced transmittance matrix approach," J. Opt. Soc. Am. A **12**, 1077–1086 (1995).
19. C. Wan, T. K. Gaylord, and M. S. Bakir, "RCWA-EIS method for interlayer grating coupling," Appl. Opt. **55**, 5900–5908 (2016).
20. H. Kogelnik, "Coupled wave theory for thick hologram gratings," Bell Syst. Tech. J. **48**, 2909–2947 (1969).